Logic and functional operations using a near-field optically coupled quantum-dot system

Suguru Sangu,[1,2,*] Kiyoshi Kobayashi,[1] Akira Shojiguchi,[1] and Motoichi Ohtsu[1,3]
[1]*ERATO Localized Photon Project, Japan Science and Technology Agency, 687-1 Tsuruma, Machida, Tokyo 194-0004, Japan*
[2]*Research and Development Center, Ricoh Company, Limited, 16-1 Shinei-cho, Tsuzuki-ku, Yokohama, Kanagawa 224-0035, Japan*
[3]*Interdisciplinary Graduate School of Science and Engineering, Tokyo Institute of Technology, 4259 Nagatsuta-cho, Midori-ku, Yokohama, Kanagawa 226-8502, Japan*

(Received 11 September 2003; revised manuscript received 18 November 2003; published 26 March 2004)

This paper investigates the exciton dynamics in a three-quantum-dot system coupled via an optical near field. The system consists of two identical quantum dots coupled coherently (the coherent operation part) and a third quantum dot with exciton sublevels (the output part). It provides certain characteristic functional operations depending on the initial excitation, as well as symmetry of the coupling strengths or the spatial arrangement. First, we analytically obtain the coupling strength between two quantum dots via an optical near field and give a numerical estimation for a CuCl quantum-cube system. Then, a resonance condition between the two parts is shown; this depends on the initial excitation in the coherent operation part. Using this condition, which can be realized by adjusting the energy level of a quantum dot in the output part, AND- and XOR-logic operations can be demonstrated in a symmetrically arranged quantum-dot system. We also discuss how the asymmetry of the system affects the energy transfer through certain coupled states in the coherent operation part that would be forbidden in a symmetrically arranged system. Although the asymmetry degrades the signal contrast for logic operations, it is expected to open up new techniques for novel device technologies where quantum entangled states are mediated in the operations.

DOI: 10.1103/PhysRevB.69.115334 PACS number(s): 73.21.La, 42.79.Ta, 71.35.Gg

I. INTRODUCTION

The miniaturization of the constituents of conventional photonic devices will reach a barrier in the near future as the device integration progresses. A $10^4 \times 10^4$ matrix switch will be required to realize the necessary high data transmission rates, which are expected to reach 40 TB/s by 2015,[1] and the size of each element will become less than 100 nm, far below the diffraction limit of light. In order to overcome this barrier, *nanophotonics*, in which local electromagnetic interactions between nanometric materials and an optical near field are utilized,[2] must be promising technology. Since an optical near field is not limited by the diffraction of light, this technology is expected to enable signal transfer and control in nanometric device elements.

The characteristic features of an optical near field can be utilized to achieve functional operations in nanophotonic devices, which are discussed in this paper. One such feature is the high spatial localization, which enables us to access individual nanometric elements in devices that are smaller than the diffraction limit of light. This feature is widely used in scanning near-field optical microscopy and spectroscopy[3] for nanometric structures,[4–6] single molecules,[7] and biological specimens.[8] On the basis of the spatial localization of an optical near field, an interesting phenomenon of dipole-forbidden energy transfer has been observed experimentally in a semiconductor quantum-dot system.[9] Several theoretical studies of a few quantum-dot systems related to optical near-field techniques have been reported[10] and the dipole-forbidden transition has been also expected[11,12] by considering nonlocal susceptibility and a highly localized optical field. Another characteristic feature of an optical near field is the anomalous dispersion relation due to the coupling between the photon and the material excitation.[13] This can bring about collective dynamics inherent in optical near-field interactions in a system consisting of several nanometric materials.[14,15]

In this paper, we propose functional devices which consist of several quantum dots coupled via an optical near field. For device operations, unidirectional signal transfer from input to output terminals must occur. We previously proposed using several quantum dots to form the fundamental blocks of a nanophotonic device, in which the discrete energy levels resonantly couple with each other via an optical near field. Intra-sublevel relaxation due to exciton-phonon coupling in a quantum dot guarantees unidirectional energy transfer. A nanophotonic switch has been studied both experimentally[16] and theoretically[17,18] using such a coupled quantum-dot system, and a switch was recently demonstrated using CuCl quantum cubes.[16] In such nanophotonic devices using the resonant energy transfer, quantum coherence survives for a short period of time; afterwards, the excitation moves in a lower-energy state.[19] The proposed coupled quantum-dot system consists of two characteristic parts similar to the nanophotonic switch mentioned above: one is the portion of the near-field optically coupled nanometric materials that maintains quantum coherence, which we call the *coherent operation part*; and the other determines certain final states with dissipation or decoherence, which we call the *output part*. This paper focuses on taking full advantage of these coherent and defined output parts to achieve functional operations. As a typical example, we consider the three-quantum-dot system illustrated in Fig. 1, where the excitons are carriers for the signal transfer. In the system, two identical quantum dots (QD-A and -B) are resonantly coupled with each other via an optical near field.

Various authors have investigated the coupling properties and dynamics in a pair of quantum dots. For example, the

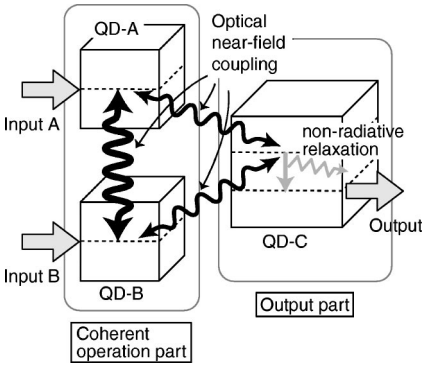

FIG. 1. Illustration of a three-quantum-dot system that consists of two identical two-level dots (QD-A and -B) and a three-level dot (QD-C). Since the coupling between QD-A and -B is stronger than that between QD-A and C (QD-B and -C), the system is divided into two parts: a coherent operation part with optical nutation, and an output part with a dissipation process.

energy shift due to exciton-exciton or Coulomb interactions between electrons and holes has been evaluated theoretically to process quantum information,[20,21] and a controlled-NOT logic gate has been proposed using the energy shift.[22] In these studies, excitons or qubits were controlled by two-color laser pulses of far-field light. As a similar subject to this paper, Quiroga and Johnson[23] theoretically discussed the dynamics in two- and three-quantum-dot systems and presented a way to prepare both quantum Bell and Greenberger-Horne-Zeilinger entangled states, by using far-field light, which allows only global excitation of two and three quantum dots with spatially symmetric arrangement. By contrast, we deal with coupled quantum-dot systems arranged symmetrically and asymmetrically, which are individually excited by the optical near field, and the intra-sublevel relaxation is also considered for the unidirectional energy transfer. Note that the excitation in each quantum dot can be prepared individually owing to the spatial localization of the optical near field. The exciton dynamics driven by the optical near field has been investigated in the case of a coupled two-quantum-dot system with a relaxation process.[17] The energy transfer between two quantum dots is expressed as a Förster process,[24] and the nutation of excitation occurs in the strongly coupled or resonant energy levels, corresponding to the coherent operation part in our system. For the short period before relaxation, certain coherently coupled states appear in the coherent operation part, depending on the initial excitation. In order to prepare the initial excitation, the shorter excitation time in the individual quantum dot than the energy-transfer time between two identical quantum dots is necessary, where the excitation time is inversely proportional to the optical near-field intensity. The energy-transfer time or coupling strength via an optical near field can be controlled by adjusting interdot spacings. The population in the coherently coupled states can be transferred to the third quantum dot (QD-C) if the energy level of QD-C is adjusted to couple resonantly with the entangled states in the coherent operation part. If this happens, QD-C operates as the output part, which involves an intra-sublevel relaxation process due to the exciton-phonon interaction. In this manner, unidirectional energy or signal transfer is satisfied.

This paper examines the exciton dynamics in this system illustrated in Fig. 1 using density-matrix formalism. The dynamics of the system can be determined analytically when three quantum dots are arranged symmetrically. AND- and XOR-logic operations can also be demonstrated by adjusting the energy configuration in this three-quantum-dot system. The asymmetry due to the coupling strength of the quantum-dot pairs via an optical near field or quantum-dot arrangement also plays an important role in the exciton dynamics. We find that an asymmetric arrangement permits energy transfer from the coherent operation part to the output part via a certain quantum entangled state, the so-called ''dark state''[25] in a symmetric system. This characteristic feature due to the spatial arrangement may be useful for detection of quantum entangled state. Here, note that these logic and functional operations are in the irreversible process, although quantum entangled states are partially mediated to sort out the initial excitations. This resembles quantum information processing, however, we do not need long coherence time as the quantum computation requires. Regarding quantum information processing with dissipation or decoherence, there are several reports which are discussed such as tolerance and decoherence-free operations.[26,27]

This paper is organized as follows. Section II derives the optical near-field coupling between two energy levels in two quantum dots and shows the existence of dipole-forbidden energy transfer mediated by an optical near field. The coupling strength is also estimated numerically and is used to discuss the exciton dynamics in a three-quantum-dot system. Section III is devoted to the formulation of the exciton dynamics in the relevant system using density-matrix formalism. Here, we present the ''selective'' energy transfer from the coherent operation part to the output part. Based on this feature, we show that logic operations can be realized in a symmetrically arranged quantum-dot system. Section IV discusses the effects of the asymmetry using the numerical exciton dynamics results. Finally, concluding remarks are given in Sec. V.

II. OPTICAL NEAR-FIELD COUPLING

In this section, we formulate an optical near-field coupling between two quantum dots using the multipolar QED Hamiltonian[28,29] in the dipole approximation, $\boldsymbol{\mu}\cdot\boldsymbol{D}$, where $\boldsymbol{\mu}$ and $\boldsymbol{D}$ represent the transition dipole moment and electric displacement field, respectively. There are several advantages to use the multipolar QED Hamiltonian instead of the minimal coupling Hamiltonian $\boldsymbol{p}\cdot\boldsymbol{A}$, $\boldsymbol{p}$ being the electronic momentum and $\boldsymbol{A}$ the vector potential; first of all, the multipolar QED Hamiltonian does not contain any explicit intermolecular or inter-quantum-dot Coulomb interactions in the interaction Hamiltonian and entire contribution to the fully retarded result originates from exchange of transverse photons, while in the minimal coupling, the intermolecular interactions arise both from exchange of transverse photons, which include static components, and from instantaneous intermolecular electrostatic interactions.[30] Second, it clarifies

physical interpretation of the dipole-forbidden transition via the optical near field as discussed below. Basic ideas in the formulation are to express internal electronic structures in a quantum dot regarding them as collection of local dipoles and to investigate the interactions between nanometric materials and spatially varied optical near fields. We can also depict multipoles for a single quantum dot by using an effective-mass approximation. Such theoretical approach has been already published[31] where the enhancement of electric quadrupole coupling was pointed out by assuming steep variation of electric field due to the optical near field. This phenomenon is equivalent to our result of the dipole-forbidden transition, but the field variation in our theoretical formulation is caused by the coupling between the local dipoles in the neighboring quantum-dot pair [see Fig. 2(b)].

In the following sections, we present the interaction Hamiltonian in second-quantized form in terms of electron basis functions satisfying the quantum-dot boundary conditions, as well as transition dipole moments of excitons, and derive an optical near-field coupling on the basis of the projection operator method we previously proposed.

A. Interaction Hamiltonian

According to the dipole coupling in the multipolar Hamiltonian, the interaction between photons and nanometric materials can be written as[29]

$$\hat{H}_{\rm int} = -\int \psi^{\dagger}(\boldsymbol{r})\boldsymbol{\mu}(\boldsymbol{r})\psi(\boldsymbol{r})\cdot\hat{\boldsymbol{D}}(\boldsymbol{r})d\boldsymbol{r}, \tag{1}$$

where $\psi^{\dagger}(\boldsymbol{r})$ and $\psi(\boldsymbol{r})$ denote field operators for electron creation and annihilation, respectively, and the dipole moment and the second-quantized electric displacement vector at position $\boldsymbol{r}$ are expressed as $\boldsymbol{\mu}(\boldsymbol{r})$ and $\hat{\boldsymbol{D}}(\boldsymbol{r})$, respectively. In a quantum dot, the electron field operators should be expanded in terms of basis functions $\phi_{\nu\boldsymbol{n}}(\boldsymbol{r})$ that satisfy the electron boundary conditions in a quantum dot, which is analogous to those in bulk materials where the Bloch functions satisfying periodic boundary condition are used. The field operators are given by

$$\psi(\boldsymbol{r}) = \sum_{\nu=c,v}\sum_{\boldsymbol{n}} \hat{c}_{\nu\boldsymbol{n}}\phi_{\nu\boldsymbol{n}}(\boldsymbol{r}), \quad \psi^{\dagger}(\boldsymbol{r}) = \sum_{\nu=c,v}\sum_{\boldsymbol{n}} \hat{c}^{\dagger}_{\nu\boldsymbol{n}}\phi^{*}_{\nu\boldsymbol{n}}(\boldsymbol{r}), \tag{2}$$

where $\hat{c}^{\dagger}_{\nu\boldsymbol{n}}$ and $\hat{c}_{\nu\boldsymbol{n}}$ represent the creation and annihilation operators for the electrons specified by $(\nu,\boldsymbol{n})$, respectively, and the indices $\nu=c,v$ denote the conduction and valence bands. The discrete energy levels in the quantum dot are labeled $\boldsymbol{n}$. The basis functions satisfy the following completeness condition, as well as orthonormalization:

$$\sum_{\nu=c,v}\sum_{\boldsymbol{n}} \phi^{*}_{\nu\boldsymbol{n}}(\boldsymbol{r})\phi_{\nu\boldsymbol{n}}(\boldsymbol{r}') = \delta(\boldsymbol{r}-\boldsymbol{r}'). \tag{3}$$

Simultaneously, we express the electric displacement vector $\hat{\boldsymbol{D}}(\boldsymbol{r})$ using exciton-polariton creation and annihilation operators $(\hat{\xi}^{\dagger}_{\boldsymbol{k}},\hat{\xi}_{\boldsymbol{k}})$, where branch suffix of the exciton-polariton is suppressed by taking only an upper branch. We consider exciton-polaritons because a nanometric system in a near-field optical environment is always surrounded by macroscopic materials, such as the substrate, matrix, fiber probe, and so on. Previously,[13,32] we proposed an effective interaction for such a nanometric system mediated by exciton-polaritons that are expressed in mixed states between photons and macroscopic material excitations instead of free photons. We showed that such a treatment provides a good description of the characteristics of an optical near field.[33] Using this, the electric displacement vector $\hat{\boldsymbol{D}}(\boldsymbol{r})$ in Eq. (1) can be written as[34]

$$\hat{\boldsymbol{D}}(\boldsymbol{r}) = i\sqrt{\frac{2\pi}{V}}\sum_{\boldsymbol{k}}\sum_{\lambda=1}^{2} \boldsymbol{e}_{\lambda}(\boldsymbol{k})f(k)(\hat{\xi}_{\boldsymbol{k}}e^{i\boldsymbol{k}\cdot\boldsymbol{r}} - \hat{\xi}^{\dagger}_{\boldsymbol{k}}e^{-i\boldsymbol{k}\cdot\boldsymbol{r}}), \tag{4}$$

with

$$f(k) = \frac{\hbar ck}{\sqrt{E(k)}}\sqrt{\frac{E^2(k)-E_m^2}{2E^2(k)-E_m^2-\hbar^2c^2k^2}}, \tag{5}$$

where $\hbar$, V, $\boldsymbol{e}_{\lambda}(\boldsymbol{k})$, and $\boldsymbol{k}$ are the Dirac constant, the quantization volume, the unit polarization vector, and the wave vector of the exciton-polaritons, respectively. Here we assume $\boldsymbol{e}_{\lambda}(\boldsymbol{k})$ as real. The speed of light in a vacuum is c, and the exciton-polariton energy with a wave vector $\boldsymbol{k}$ and the macroscopic material excitation energy are $E(k)$ and E_m, respectively. Substituting Eqs. (2) and (4) into Eq. (1) gives the interaction Hamiltonian in the second-quantized representation as

$$\hat{H}_{\rm int} = \sum_{\nu\boldsymbol{n}\nu'\boldsymbol{n}'\boldsymbol{k}\lambda} (\hat{c}^{\dagger}_{\nu\boldsymbol{n}}\hat{c}_{\nu'\boldsymbol{n}'}\hat{\xi}_{\boldsymbol{k}}g_{\nu\boldsymbol{n}\nu'\boldsymbol{n}'\boldsymbol{k}\lambda} - \hat{c}^{\dagger}_{\nu\boldsymbol{n}}\hat{c}_{\nu'\boldsymbol{n}'}\hat{\xi}^{\dagger}_{\boldsymbol{k}}g_{\nu\boldsymbol{n}\nu'\boldsymbol{n}'-\boldsymbol{k}\lambda}), \tag{6}$$

with

$$g_{\nu\boldsymbol{n}\nu'\boldsymbol{n}'\boldsymbol{k}\lambda} = -i\sqrt{\frac{2\pi}{V}}f(k)\int \phi^{*}_{\nu\boldsymbol{n}}(\boldsymbol{r}) \times[\boldsymbol{\mu}(\boldsymbol{r})\cdot\boldsymbol{e}_{\lambda}(\boldsymbol{k})]e^{i\boldsymbol{k}\cdot\boldsymbol{r}}\phi_{\nu'\boldsymbol{n}'}(\boldsymbol{r})d\boldsymbol{r}. \tag{7}$$

B. Transition moments for exciton states

In order to describe the creation and annihilation of excitons in a quantum dot, it is convenient to use the Wannier representation in which electrons are localized in an atomic site $\boldsymbol{R}$. Then, the electron field operators can be expanded using the Wannier functions $w_{\nu\boldsymbol{R}}(\boldsymbol{r})$ instead of $\phi_{\nu\boldsymbol{n}}(\boldsymbol{r})$,

$$\psi(\boldsymbol{r}) = \sum_{\nu=c,v}\sum_{\boldsymbol{R}} \hat{c}_{\nu\boldsymbol{R}}w_{\nu\boldsymbol{R}}(\boldsymbol{r}), \quad \psi^{\dagger}(\boldsymbol{r}) = \sum_{\nu=c,v}\sum_{\boldsymbol{R}} \hat{c}^{\dagger}_{\nu\boldsymbol{R}}w^{*}_{\nu\boldsymbol{R}}(\boldsymbol{r}), \tag{8}$$

where $c^{\dagger}_{\nu\boldsymbol{R}}$ and $c_{\nu\boldsymbol{R}}$ denote the creation and annihilation operators of electrons at site $\boldsymbol{R}$ in the energy band ν. These operators in the Wannier representation are written in terms of $\hat{c}_{\nu\boldsymbol{n}}$ in Eq. (2) as follows:

$$\hat{c}_{\nu \boldsymbol{R}} = \sum_{\nu'=c,v} \sum_{\boldsymbol{n}} \hat{c}_{\nu' \boldsymbol{n}} \int w^*_{\nu \boldsymbol{R}}(\boldsymbol{r}) \phi_{\nu' \boldsymbol{n}}(\boldsymbol{r}) d\boldsymbol{r},$$

$$\hat{c}^\dagger_{\nu \boldsymbol{R}} = \sum_{\nu'=c,v} \sum_{\boldsymbol{n}} \hat{c}^\dagger_{\nu' \boldsymbol{n}} \int w_{\nu \boldsymbol{R}}(\boldsymbol{r}) \phi^*_{\nu' \boldsymbol{n}}(\boldsymbol{r}) d\boldsymbol{r}. \tag{9}$$

When we assume excitons in the weak-confinement regime, i.e., an exciton Bohr radius to be smaller than the quantum-dot size, the exciton states in a quantum dot specified by the quantum number $\boldsymbol{m}$ and μ can be described by superposition of the excitons in the Wannier representation as[35]

$$|\Phi_{\boldsymbol{m}\mu}\rangle = \sum_{\boldsymbol{R},\boldsymbol{R}'} F_{\boldsymbol{m}}(\boldsymbol{R}_{\text{c.m.}}) \varphi_\mu(\boldsymbol{\beta}) \hat{c}^\dagger_{c\boldsymbol{R}'} \hat{c}_{v\boldsymbol{R}} |\Phi_g\rangle,$$

$$= \sum_{\boldsymbol{R},\boldsymbol{R}'} F_{\boldsymbol{m}}(\boldsymbol{R}_{\text{c.m.}}) \varphi_\mu(\boldsymbol{\beta}) \sum_{\boldsymbol{n},\boldsymbol{n}'} h_{\boldsymbol{R}n\boldsymbol{R}'\boldsymbol{n}'} \hat{c}^\dagger_{c\boldsymbol{n}} \hat{c}_{v\boldsymbol{n}'} |\Phi_g\rangle, \tag{10}$$

where $F_{\boldsymbol{m}}(\boldsymbol{R}_{\text{c.m.}})$ and $\varphi_\mu(\boldsymbol{\beta})$ denote the envelope functions for the center of mass and relative motions of the excitons, respectively. These are $\boldsymbol{R}_{\text{c.m.}} = (m_e \boldsymbol{R}' + m_h \boldsymbol{R})/(m_e + m_h)$ and $\boldsymbol{\beta} = \boldsymbol{R}' - \boldsymbol{R}$, where m_e and m_h are the effective masses of the electrons and holes. The overlap integrals $h_{\boldsymbol{R}n\boldsymbol{R}'\boldsymbol{n}'}$ are defined as

$$h_{\boldsymbol{R}n\boldsymbol{R}'\boldsymbol{n}'} = \int \int w^*_{v\boldsymbol{R}}(\boldsymbol{r}_2) w_{c\boldsymbol{R}'}(\boldsymbol{r}_1) \phi^*_{c\boldsymbol{n}}(\boldsymbol{r}_1) \phi_{v\boldsymbol{n}'}(\boldsymbol{r}_2) d\boldsymbol{r}_1 d\boldsymbol{r}_2. \tag{11}$$

The sum of ν' in Eq. (9) is determined automatically as $\hat{c}^\dagger_{c\boldsymbol{n}}$ and $\hat{c}_{v\boldsymbol{n}'}$ because the valence band is fully occupied in the initial ground state $|\Phi_g\rangle$. Using Eqs. (6) and (10), the transition moment from the exciton state to the ground state is obtained as

$$\langle \Phi_g | \hat{H}_{\text{int}} | \Phi_{\boldsymbol{m}\mu} \rangle = \sum_{\boldsymbol{n}_1,\boldsymbol{n}_2} \sum_{\boldsymbol{R},\boldsymbol{R}'} F_{\boldsymbol{m}}(\boldsymbol{R}_{\text{c.m.}}) \varphi_\mu(\boldsymbol{\beta}) \times \sum_{\boldsymbol{k}} \sum_{\lambda=1}^{2} (\hat{\xi}_{\boldsymbol{k}} g_{v\boldsymbol{n}_1 c\boldsymbol{n}_2 \boldsymbol{k}\lambda} - \hat{\xi}^\dagger_{\boldsymbol{k}} g_{v\boldsymbol{n}_1 c\boldsymbol{n}_2 - \boldsymbol{k}\lambda}) \times h_{\boldsymbol{R}\boldsymbol{n}_2\boldsymbol{R}'\boldsymbol{n}_1}, \tag{12}$$

where we use the following relation:

$$\langle \Phi_g | \hat{c}^\dagger_{v\boldsymbol{n}_1} \hat{c}_{c\boldsymbol{n}_2} \hat{c}^\dagger_{c\boldsymbol{n}_3} \hat{c}_{v\boldsymbol{n}_4} | \Phi_g \rangle = \delta_{\boldsymbol{n}_1\boldsymbol{n}_4} \delta_{\boldsymbol{n}_2\boldsymbol{n}_3}. \tag{13}$$

In addition, with the help of the completeness and orthonormalization of $\phi_{\nu\boldsymbol{n}}(\boldsymbol{r})$ [see Eq. (3)], we can simplify the product of g and h as

$$\sum_{\boldsymbol{n}_1,\boldsymbol{n}_2} g_{v\boldsymbol{n}_1 c\boldsymbol{n}_2 k\lambda} h_{\boldsymbol{R}\boldsymbol{n}_2\boldsymbol{R}'\boldsymbol{n}_1} = -i\sqrt{\frac{2\pi}{V}} f(k) \int w^*_{v\boldsymbol{R}}(\boldsymbol{r}) \boldsymbol{\mu}(\boldsymbol{r}) w_{c\boldsymbol{R}'}(\boldsymbol{r}) \cdot \boldsymbol{e}_\lambda(\boldsymbol{k}) e^{i\boldsymbol{k}\cdot\boldsymbol{r}} d\boldsymbol{r}$$

$$\approx -i\sqrt{\frac{2\pi}{V}} f(k) [\boldsymbol{\mu}_{cv} \cdot \boldsymbol{e}_\lambda(\boldsymbol{k})] e^{i\boldsymbol{k}\cdot\boldsymbol{R}} \delta_{\boldsymbol{R}\boldsymbol{R}'}, \tag{14}$$

where the transformation of the spatial integral in the first line of Eq. (14) into the sum of the unit cells and the spatial localization of the Wannier functions provides $\delta_{\boldsymbol{R}\boldsymbol{R}'}$ in the second line. The transition dipole moment for each unit cell is defined as

$$\boldsymbol{\mu}_{cv} = \int_{\text{UC}} w^*_{v\boldsymbol{R}}(\boldsymbol{r}) \boldsymbol{\mu}(\boldsymbol{r}) w_{c\boldsymbol{R}}(\boldsymbol{r}) d\boldsymbol{r}. \tag{15}$$

We assume that the transition dipole moment is the same as that of the bulk material, independent of the site $\boldsymbol{R}$, and that the electric displacement vector is uniform at each site. Finally, Eq. (12) is reduced to

$$\langle \Phi_g | \hat{H}_{\text{int}} | \Phi_{\boldsymbol{m}\mu} \rangle = -i\sqrt{\frac{2\pi}{V}} \sum_{\boldsymbol{R}} \sum_{\boldsymbol{k}} \sum_{\lambda=1}^{2} f(k) \times [\boldsymbol{\mu}_{cv} \cdot \boldsymbol{e}_\lambda(\boldsymbol{k})] F_{\boldsymbol{m}}(\boldsymbol{R}) \varphi_\mu(0) \times (\hat{\xi}_{\boldsymbol{k}} e^{i\boldsymbol{k}\cdot\boldsymbol{R}} - \hat{\xi}^\dagger_{\boldsymbol{k}} e^{-i\boldsymbol{k}\cdot\boldsymbol{R}}). \tag{16}$$

Here, we note that the exciton-polariton field expanded by the plane wave with the wave vector $\boldsymbol{k}$ depends on the site $\boldsymbol{R}$ in the quantum dot because we do not apply the long-wave approximation that is usually used for far-field light.

C. Optical near-field coupling

To derive the coupling strength between two quantum dots due to the optical near-field interaction, we use the projection operator method, which was reported in detail in our previous paper.[32] In this method, the eigenstates of a total optical near-field system are divided into two subspaces: a relevant P space constructed from the two energy levels for each quantum dot and the exciton-polariton vacuum state, and an irrelevant Q space that is complementary to the P space and includes exciton-polariton states. Using this formulation, the coupling strength is given to the lowest order as

$$\hbar U = \sum_m \langle \Psi^P_f | \hat{H}_{\text{int}} | m^Q \rangle \langle m^Q | \hat{H}_{\text{int}} | \Psi^P_i \rangle \times \left(\frac{1}{E^P_{0i} - E^Q_{0m}} + \frac{1}{E^P_{0f} - E^Q_{0m}} \right), \tag{17}$$

where E^P_{0i}, E^P_{0f}, and E^Q_{0m} represent the eigenenergies of the unperturbed Hamiltonian for the initial and final states in P space and the intermediate state in Q space, respectively. Since we focus on the interdot interaction of Eq. (17), we set the initial and final states in P space to $|\Psi^P_i\rangle$

$=|\Phi^A_{\mathbf{m}\mu}\rangle|\Phi^B_g\rangle|0\rangle$ and $|\Psi^P_f\rangle=|\Phi^A_g\rangle|\Phi^B_{\mathbf{m}'\mu'}\rangle|0\rangle$. Then, the intermediate states in Q space that involve exciton-polaritons with the wave vector $\boldsymbol{k}$ are utilized for the energy transfer from one quantum dot to the other, according to $|m^Q\rangle=|\Phi^A_g\rangle|\Phi^B_g\rangle|\boldsymbol{k}\rangle$ and $|\Phi^A_{\mathbf{m}\mu}\rangle|\Phi^B_{\mathbf{m}'\mu'}\rangle|\boldsymbol{k}\rangle$. The superscripts A and B are used to label two quantum dots. Substituting Eq. (16), one can rewrite Eq. (17) as

$$\hbar U=\varphi^A_\mu(0)\varphi^{B*}_{\mu'}(0)\int\int F^A_{\mathbf{m}}(\boldsymbol{R}_A)F^{B*}_{\mathbf{m}'}(\boldsymbol{R}_B)[Y_A(\boldsymbol{R}_A-\boldsymbol{R}_B)+Y_B(\boldsymbol{R}_A-\boldsymbol{R}_B)]d\boldsymbol{R}_A d\boldsymbol{R}_B, \tag{18}$$

where the sum of $\boldsymbol{R}_\alpha$ ($\alpha=A,B$) in Eq. (16) is transformed to the integral form. The functions $Y_\alpha(\boldsymbol{R}_{AB})$, which connect the spatially isolated two envelope functions $F^A_{\mathbf{m}}(\boldsymbol{R}_A)$ and $F^B_{\mathbf{m}}(\boldsymbol{R}_B)$, are defined as

$$Y_\alpha(\boldsymbol{R}_{AB})=-\frac{1}{4\pi^2}\sum_{\lambda=1}^{2}\int[\boldsymbol{\mu}^A_{cv}\cdot\hat{\boldsymbol{e}}_\lambda(\boldsymbol{k})][\boldsymbol{\mu}^B_{cv}\cdot\hat{\boldsymbol{e}}_\lambda(\boldsymbol{k})]f^2(k)\times\left(\frac{e^{i\boldsymbol{k}\cdot\boldsymbol{R}_{AB}}}{E(k)+E_\alpha}+\frac{e^{-i\boldsymbol{k}\cdot\boldsymbol{R}_{AB}}}{E(k)-E_\alpha}\right)d\boldsymbol{k}, \tag{19}$$

where $\boldsymbol{R}_{AB}=\boldsymbol{R}_A-\boldsymbol{R}_B$ is used. In order to obtain an explicit functional form of $Y_\alpha(\boldsymbol{R}_{AB})$, we apply the effective-mass approximation to the exciton-polaritons,

$$E(k)=\frac{\hbar^2k^2}{2m_p}+E_m, \tag{20}$$

where m_p is the exciton-polariton effective mass. Using this approximation, Eq. (19) can be transformed into

$$\begin{aligned}Y_\alpha(\mathbf{R}_{AB})=&(\boldsymbol{\mu}^A_{cv}\cdot\boldsymbol{\mu}^B_{cv})\left[W_{\alpha+}e^{-\Delta_{\alpha+}R_{AB}}\left(\frac{\Delta^2_{\alpha+}}{R_{AB}}+\frac{\Delta_{\alpha+}}{R^2_{AB}}+\frac{1}{R^3_{AB}}\right)-W_{\alpha-}e^{-\Delta_{\alpha-}R_{AB}}\left(\frac{\Delta^2_{\alpha-}}{R_{AB}}+\frac{\Delta_{\alpha-}}{R^2_{AB}}+\frac{1}{R^3_{AB}}\right)\right]\\&-(\boldsymbol{\mu}^A_{cv}\cdot\hat{\mathbf{R}}_{AB})(\boldsymbol{\mu}^B_{cv}\cdot\hat{\mathbf{R}}_{AB})\left[W_{\alpha+}e^{-\Delta_{\alpha+}R_{AB}}\times\left(\frac{\Delta^2_{\alpha+}}{R_{AB}}+\frac{3\Delta_{\alpha+}}{R^2_{AB}}+\frac{3}{R^3_{AB}}\right)-W_{\alpha-}e^{-\Delta_{\alpha-}R_{AB}}\left(\frac{\Delta^2_{\alpha-}}{R_{AB}}+\frac{3\Delta_{\alpha-}}{R^2_{AB}}+\frac{3}{R^3_{AB}}\right)\right],\end{aligned} \tag{21}$$

where R_{AB} and $\hat{\mathbf{R}}_{AB}$ are the absolute value $|\boldsymbol{R}_{AB}|$ and the unit vector defined by $\boldsymbol{R}_{AB}/R_{AB}$, respectively. The weight coefficients $W_{\alpha\pm}$ and decay constants $\Delta_{\alpha\pm}$ are given by

$$W_{\alpha_\pm}=\frac{E_p}{E_\alpha}\frac{(E_m-E_\alpha)(E_m+E_\alpha)}{(E_m-E_p\mp E_\alpha)(E_m\pm E_\alpha)-E^2_m/2},$$

$$\Delta_{\alpha_\pm}=\frac{1}{\hbar c}\sqrt{E_p(E_m\pm E_\alpha)}, \tag{22}$$

where the exciton-polariton effective mass is rewritten as $E_p=m_pc^2$. Since the dipole moments $\boldsymbol{\mu}^A_{cv}$ and $\boldsymbol{\mu}^B_{cv}$ are not determined as fixed values, we assume that they are parallel, and take a rotational average of Eq. (21). Therefore, $\langle(\boldsymbol{\mu}^A_{cv}\cdot\hat{\mathbf{R}}_{AB})(\boldsymbol{\mu}^B_{cv}\cdot\hat{\mathbf{R}}_{AB})\rangle=\mu^A_{cv}\mu^B_{cv}/3$ with $\mu^\alpha_{cv}=|\boldsymbol{\mu}^\alpha_{cv}|$, and we obtain the final form of the function $Y_\alpha(R_{AB})$ as

$$Y_\alpha(R_{AB})=\frac{2\mu^A_{cv}\mu^B_{cv}}{3R_{AB}}(W_{\alpha+}\Delta^2_{\alpha+}e^{-\Delta_{\alpha+}R_{AB}}-W_{\alpha-}\Delta^2_{\alpha-}e^{-\Delta_{\alpha-}R_{AB}}). \tag{23}$$

Equation (23) is the sum of two Yukawa functions with a short and long interaction range (heavy and light effective mass) given by the second equation in Eq. (22). We can estimate the coupling strength between two quantum dots from the analytic form of the interaction potential given by Eqs. (18) and (23), and we can show the existence of dipole-forbidden energy transfer driven by the optical near-field coupling, as discussed in the following section.

D. Numerical results

In this section, we give typical values of the coupling strength of $\hbar U$ in Eq. (18) using an example of CuCl quantum cubes embedded in a NaCl matrix. Due to the effect of size confinement, the center-of-mass motion and relative motion for an exciton in a CuCl quantum cube are[35]

$$F^\alpha_{\mathbf{m}}(\boldsymbol{R}_\alpha)=\left(\frac{2}{L_\alpha}\right)^{3/2}\sin\left(\frac{\pi m_x x_\alpha}{L_\alpha}\right)\sin\left(\frac{\pi m_y y_\alpha}{L_\alpha}\right)\sin\left(\frac{\pi m_z z_\alpha}{L_\alpha}\right),$$

$$\varphi_{1s}(r)=\frac{1}{\sqrt{\pi a^3}}e^{-r/a}, \tag{24}$$

respectively, where the atomic site and the quantum number are represented by $\boldsymbol{R}_\alpha=(x_\alpha,y_\alpha,z_\alpha)$ with $\alpha=A,B$ and $\boldsymbol{m}=(m_x,m_y,m_z)$ with $m_x,m_y,m_z=1,2,3,\ldots$. The variables L_α and a denote a width of the quantum cube and the Bohr radius of the exciton, respectively. Here, we assume relative motion in the $1s$ state. The coupling strength is obtained numerically by substituting Eqs. (23) and (24) into Eq. (18). In Fig. 2(a), the calculation results are plotted as a function of the intercube distance. The curve with square dots represents the coupling between the dipole-active exciton levels, i.e., $\boldsymbol{m}=\boldsymbol{m}'=(1,1,1)$, in two quantum cubes. When we set the intercube distance and a width of the quantum cubes as $d=5$ nm and $L_A=L_B=10$ nm, respectively, which corresponds to the resonant coupling between QD-A and -B in Fig. 1, the coupling strength is about 89 μeV ($U^{-1}=7.4$ ps). The curve with circular dots is the result for $\boldsymbol{m}=(1,1,1)$ and $\boldsymbol{m}'=(2,1,1)$. For conventional far-field light, $\boldsymbol{m}'=(2,1,1)$ is the dipole-forbidden exciton level, and it follows that the optical near-field interaction inherently involves such a transition because of the finite interaction range. Figure 2(b) is a schematic illustration of the dipole-forbidden transition, in which the optical near field enables to excite the local dipoles at the near side in a quantum dot with dipole-forbidden level for far-field light. This coupling

strength is estimated from Fig. 2(a) as $\hbar U=37\ \mu$eV ($U^{-1}=17.7$ ps) for $d=5$ nm, and $\hbar U=14\ \mu$eV ($U^{-1}=46.9$ ps) for $d=15$ nm, where the cube sizes are set as $L_A=10$ nm and $L_B=14.1$ nm to realize resonant energy transfer between the two quantum cubes. The coupling strength ($\boldsymbol{m}\neq\boldsymbol{m}'$) is approximately half that of $\boldsymbol{m}=\boldsymbol{m}'$ at the same intercube distance, but it is strong enough for our proposed nanophotonic devices. For functional operations, the difference between the coupling strengths can be used to divide the system into two parts, i.e., the coherent operation and the output parts. Therefore, in the following discussion of the functional operations, we use $d=5$ nm as the values of the coupling strength between QD-A and B, and $d=15$ nm for that between QD-A and C or QD-B and C.

III. EXCITON DYNAMICS AND THEIR APPLICATION TO FUNCTIONAL OPERATIONS

A. Symmetric and antisymmetric states

In this section, we discuss the exciton dynamics in a symmetrically arranged three-quantum-dot system, as shown in Fig. 1. The asymmetric effects on the dynamics are considered in the subsequent section. From the symmetry of the system, the following bases are suitable for describing the dynamics using the smallest number of density-matrix elements[36]:

$$|S_1\rangle=\frac{1}{\sqrt{2}}(|A^*BC_1C_2\rangle+|AB^*C_1C_2\rangle),$$

$$|A_1\rangle=\frac{1}{\sqrt{2}}(|A^*BC_1C_2\rangle-|AB^*C_1C_2\rangle),$$

$$|P_1'\rangle=|ABC_1C_2^*\rangle,\quad |P_1\rangle=|ABC_1^*C_2\rangle. \tag{25}$$

One-exciton state describes the condition whereby an exciton exists in either one of the three quantum dots. The ground and exciton states in each quantum dot, written using $|\Phi_g^\alpha\rangle$ and $|\Phi_{\boldsymbol{m}(1s)}^\alpha\rangle$ in the preceding section, are represented here simply as A, B, C_i ($i=1,2$), and A^*, B^*, C_i^*, respectively. Similarly, a *two-exciton state* indicates that two excitons stay in the system. The suitable bases for the two-exciton states without occupation of the lower energy level in QD-C are expressed as

$$|S_2'\rangle=\frac{1}{\sqrt{2}}(|A^*BC_1C_2^*\rangle+|AB^*C_1C_2^*\rangle),$$

$$|A_2'\rangle=\frac{1}{\sqrt{2}}(|A^*BC_1C_2^*\rangle-|AB^*C_1C_2^*\rangle),$$

$$|P_2'\rangle=|A^*B^*C_1C_2\rangle, \tag{26}$$

and those with occupation of the lower energy level are expressed as

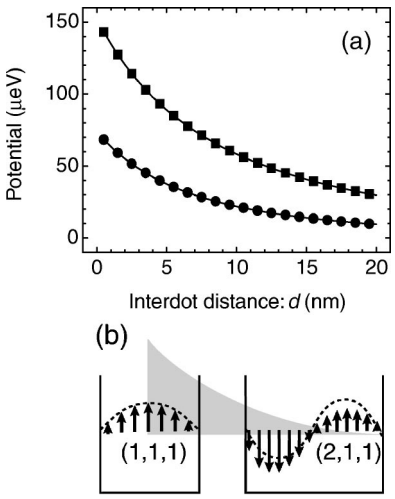

FIG. 2. (a) Optical near-field interaction potential for pairs of CuCl quantum cubes embedded in a NaCl matrix. The curves shown with square and circular dots correspond to quantum numbers for the exciton center-of-mass motion $\boldsymbol{m}=\boldsymbol{m}'=(1,1,1)$, and $\boldsymbol{m}=(1,1,1)$ and $\boldsymbol{m}'=(2,1,1)$, respectively. The energy level $\boldsymbol{m}'=(2,1,1)$ is a dipole-forbidden state for conventional far-field light. The parameters are set to $E_A=E_B=3.22$ eV, $E_m=6.9$ eV, $\mu_{cv}^A=\mu_{cv}^B=1.73\times10^{-2}$ (eV nm^3)$^{1/2}$, $L_A=10$ nm, $L_B=10$ and 14.1 nm [$\boldsymbol{m}'=(1,1,1)$ and $(2,1,1)$], and $a=0.67$ nm. (b) Schematic illustration of a transition between dipole-allowed and dipole-forbidden states via the optical near-field coupling. Steeply gradient optical near field enables to excite near side local dipoles in a quantum dot with dipole-forbidden (2,1,1) level.

$$|S_2\rangle=\frac{1}{\sqrt{2}}(|A^*BC_1^*C_2\rangle+|AB^*C_1^*C_2\rangle),$$

$$|A_2\rangle=\frac{1}{\sqrt{2}}(|A^*BC_1^*C_2\rangle-|AB^*C_1^*C_2\rangle),$$

$$|P_2\rangle=|ABC_1^*C_2^*\rangle, \tag{27}$$

where $|S\rangle$ and $|A\rangle$ represent symmetric and antisymmetric states in the coherent operation part, respectively, and the subscripts 1 and 2 on the left-hand sides in Eqs. (25), (26), and (27) denote the one- and two-exciton states, respectively. In the following, we use these bases to evaluate the exciton dynamics in the three-quantum-dot system.

B. Equations of motion and coupling properties

Based on the results of optical near-field coupling in Sec. II, a model Hamiltonian for the system $\hat{H}$ is given by

$$\hat{H}=\hat{H}_0+\hat{H}_{\rm int},$$

$$\hat{H}_0=\hbar\Omega\hat{A}^\dagger\hat{A}+\hbar\Omega\hat{B}^\dagger\hat{B}+\hbar\sum_{i=1}^{2}\Omega_{C_i}\hat{C}_i^\dagger\hat{C}_i,$$

$$\hat{H}_{\rm int}=\hbar U(\hat{A}^\dagger\hat{B}+\hat{B}^\dagger\hat{A})+\hbar U'(\hat{B}^\dagger\hat{C}_2+\hat{C}_2^\dagger\hat{B}+\hat{C}_2^\dagger\hat{A}+\hat{A}^\dagger\hat{C}_2), \tag{28}$$

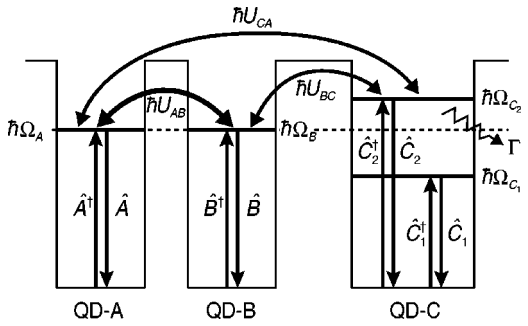

FIG. 3. Schematic drawing of exciton creation and annihilation operators and the energy-transfer process in a three-quantum-dot system. The optical near-field couplings for the quantum-dot pairs are represented by U_{AB} for QD-A and -B, U_{BC} for QD-B and -C, and U_{CA} for QD-C and -A. The nonradiative relaxation constant due to exciton-phonon coupling is denoted by Γ.

where the definitions of the creation and annihilation operators, $(\hat{A}^\dagger,\hat{A})$, $(\hat{B}^\dagger,\hat{B})$, and $(\hat{C}_i^\dagger,\hat{C}_i)$, are shown schematically in Fig. 3. The eigenfrequencies for QD-A and -B are set to $\Omega_A=\Omega_B\equiv\Omega$, and the optical near-field coupling for the symmetric system is denoted as $U_{AB}\equiv U$ and $U_{BC}=U_{CA}\equiv U'$. The equation of motion for the density operator of the quantum-dot system, $\hat{\rho}(t)$, is expressed using the Born-Markov approximation[37] as

$$\dot{\hat{\rho}}(t)=-\frac{i}{\hbar}[\hat{H}_0+\hat{H}_{\rm int},\hat{\rho}(t)]+\frac{\Gamma}{2}\{2\hat{C}_1^\dagger\hat{C}_2\hat{\rho}(t)\hat{C}_2^\dagger\hat{C}_1 - \hat{C}_2^\dagger\hat{C}_1\hat{C}_1^\dagger\hat{C}_2\hat{\rho}(t)-\hat{\rho}(t)\hat{C}_2^\dagger\hat{C}_1\hat{C}_1^\dagger\hat{C}_2\}, \quad (29)$$

where the nonradiative relaxation constant due to exciton-phonon coupling is denoted as Γ. The radiative relaxation due to exciton-free photon coupling is omitted because the time scale of the optical near-field coupling and the exciton-phonon coupling is much faster than the radiative lifetime, which is of the order of a few nanoseconds. Taking matrix elements of Eq. (29) in terms of Eqs. (25) and (26) after substituting Eq. (28) into Eq. (29), we obtain the following simultaneous differential equations:

$$\dot{\rho}_{S_1,S_1}(t)=i\sqrt{2}U'\{\rho_{S_1,P_1'}(t)-\rho_{P_1',S_1}(t)\},$$

$$\dot{\rho}_{S_1,P_1'}(t)=\left\{i(\Delta\Omega-U)-\frac{\Gamma}{2}\right\}\rho_{S_1,P_1'}(t)+i\sqrt{2}U'\{\rho_{S_1,S_1}(t)-\rho_{P_1',P_1'}(t)\},$$

$$\dot{\rho}_{P_1',S_1}(t)=\left\{-i(\Delta\Omega-U)-\frac{\Gamma}{2}\right\}\rho_{P_1',S_1}(t)-i\sqrt{2}U'\{\rho_{S_1,S_1}(t)-\rho_{P_1',P_1'}(t)\},$$

$$\dot{\rho}_{P_1',P_1'}(t)=-i\sqrt{2}U'\{\rho_{S_1,P_1'}(t)-\rho_{P_1',S_1}(t)\}-\Gamma\rho_{P_1',P_1'}(t),$$

$$\dot{\rho}_{P_1,P_1}(t)=\Gamma\rho_{P_1',P_1'}(t), \quad (30)$$

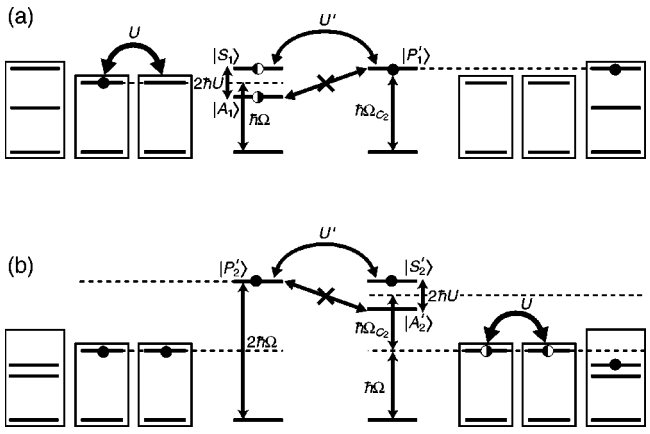

FIG. 4. Schematic explanation of selective energy transfer for (a) one- and (b) two-exciton states. The left and right illustrations represent the initial and final states, respectively. The energy transfer between states $|A\rangle$ and $|P\rangle$ is forbidden because of symmetry. Therefore, the resonance conditions for the energy transfer between states $|S\rangle$ and $|P\rangle$ are $\hbar(\Omega+U)=\hbar\Omega_{C_2}$ $(\Delta\Omega=U)$ for a one-exciton state and $2\hbar\Omega=\hbar(\Omega+\Omega_{C_2}+U)$ $(\Delta\Omega=-U)$ for a two-exciton state.

and

$$\dot{\rho}_{S_2',S_2'}(t)=i\sqrt{2}U'\{\rho_{S_2',P_2'}(t)-\rho_{P_2',S_2'}(t)\}-\Gamma\rho_{S_2',S_2'},$$

$$\dot{\rho}_{S_2',P_2'}(t)=\left\{-i(\Delta\Omega+U)-\frac{\Gamma}{2}\right\}\rho_{S_2',P_2'}(t)+i\sqrt{2}U'\{\rho_{S_2',S_2'}(t)-\rho_{P_2',P_2'}(t)\},$$

$$\dot{\rho}_{P_2',S_2'}(t)=\left\{i(\Delta\Omega+U)-\frac{\Gamma}{2}\right\}\rho_{P_2',S_2'}(t)-i\sqrt{2}U'\{\rho_{S_2',S_2'}(t)-\rho_{P_2',P_2'}(t)\},$$

$$\dot{\rho}_{P_2',P_2'}(t)=-i\sqrt{2}U'\{\rho_{S_2',P_2'}(t)-\rho_{P_2',S_2'}(t)\}, \quad (31)$$

where the density-matrix element $\langle\alpha|\hat{\rho}(t)|\beta\rangle$ is abbreviated $\rho_{\alpha,\beta}(t)$ and the energy difference $\Omega_{C_2}-\Omega$ is replaced by $\Delta\Omega$. The equations of motion in terms of the bases of Eq. (27) are not shown, but are derived similarly. Although other matrix elements related to the antisymmetric states $|A\rangle$ also appear in the equations of motion, they are decoupled from the above equations and do not affect the exciton dynamics of the symmetric states.

States $|S_1\rangle$ and $|P_1'\rangle$ or $|S_2'\rangle$ and $|P_2'\rangle$ are coherently coupled with each other, as shown by Eqs. (30) and (31). Moreover, it is noteworthy that the energy difference in Eqs. (30) and (31) makes opposite contributions to the one- and two-exciton dynamics as $\Delta\Omega-U$ and $\Delta\Omega+U$, respectively. This coupling property can be explained by considering the energy levels of a coupled system constructed from three quantum dots. Figure 4(a) shows the energy levels of a coupled system for one-exciton states. The upper and lower energy levels are split by the optical near-field coupling $\hbar U$,

corresponding to the states $|S_1\rangle$ and $|A_1\rangle$, respectively. This is confirmed by evaluating the expectation values, i.e., $\langle S_1|\hat{H}|S_1\rangle > \langle A_1|\hat{H}|A_1\rangle$. A filled circle indicates that an exciton occupies the corresponding energy level, while a semicircle indicates that an exciton exists in the energy level in either QD-A or -B with a certain probability. In order to realize the resonant energy transfer into the output part via state $|P_1'\rangle$, we must set the energy level in QD-C as $\Delta\Omega = U$ to satisfy the resonance condition of states $|S_1\rangle$ and $|P_1'\rangle$. This is because the matrix element $\langle P_1'|\hat{H}_{\rm int}|A_1\rangle$ is zero, so that this transition is forbidden in symmetric systems. For the two-exciton states, one exciton is always transferred from state $|P_2'\rangle$ to states $|S_2\rangle$ and $|P_2\rangle$ via state $|S_2'\rangle$. Figure 4(b) shows the energy levels of a coupled system for states $|P_2'\rangle$ and $|S_2'\rangle$. In this case, the center of the energy splitting due to the optical near-field coupling becomes $\hbar(\Omega+\Omega_{C_2})$. Therefore, the resonance condition of states $|P_2'\rangle$ and $|S_2'\rangle$ can be fulfilled when $\Delta\Omega = -U$ is satisfied. Here, note that the coupling between states $|P_2'\rangle$ and $|A_2'\rangle$ is also forbidden by $\langle A_2'|\hat{H}_{\rm int}|P_2'\rangle = 0$. These characteristic energy transfers allow us to pick up selective information about either the one- or two-exciton states, i.e., information about the initial exciton populations in the coherent operation part. The results are utilized for the functional logic operations as discussed below.

C. Dynamics and logic operations

Analytic solutions of Eqs. (30) and (31) for typical initial conditions can be obtained readily with the help of Laplace transforms. The output population for the one-exciton state can be written as

$$\rho_{P_1,P_1}(t) = \Gamma \int^t \rho_{P_1',P_1'}(t')dt' = \frac{1}{2} + \frac{4U'^2}{\omega_+^2 - \omega_-^2}\{\cos\phi_+ \cos(\omega_+ t + \phi_+) - \cos\phi_- \cos(\omega_- t + \phi_-)\}e^{-(\Gamma/2)t}, \quad (32)$$

with

$$\omega_\pm = \frac{1}{\sqrt{2}}[(\Delta\Omega - U)^2 + W_+W_- \pm \sqrt{\{(\Delta\Omega - U)^2 + W_+^2\}\{(\Delta\Omega - U)^2 + W_-^2\}}]^{1/2},$$

$$\phi_\pm = \tan^{-1}\left(\frac{2\omega_\pm}{\Gamma}\right),$$

$$W_\pm = 2\sqrt{2}U' \pm \frac{\Gamma}{2}, \quad (33)$$

for the initial condition $\rho_{S_1,S_1}(0) = \rho_{A_1,A_1}(0) = \rho_{S_1,A_1}(0) = \rho_{A_1,S_1}(0) = 1/2$, which corresponds to the condition $\langle A^*BC_1C_2|\hat{\rho}(t)|A^*BC_1C_2\rangle = 1$ and otherwise zero. Solutions for the two-exciton states can be obtained from an equation similar to Eq. (32), except for the sign of U, i.e., with the resonance conditions inverted. The probability of an exciton occupying the lower energy level in QD-C is

$$\rho_{S_2,S_2}(t) + \rho_{P_2,P_2}(t) = \Gamma \int^t \rho_{S_2',S_2'}(t')dt' = 2\left[\frac{1}{2} + \frac{4U'^2}{\omega_+'^2 - \omega_-'^2}\{\cos\phi_+' \cos(\omega_+' t + \phi_+') - \cos\phi_-' \cos(\omega_-' t + \phi_-')\}e^{-(\Gamma/2)t}\right], \quad (34)$$

with

$$\omega_\pm' = \frac{1}{\sqrt{2}}[(\Delta\Omega + U)^2 + W_+W_- \pm \sqrt{\{(\Delta\Omega + U)^2 + W_+^2\}\{(\Delta\Omega + U)^2 + W_-^2\}}]^{1/2},$$

$$\phi_\pm' = \tan^{-1}\left(\frac{2\omega_\pm'}{\Gamma}\right), \quad (35)$$

where the factor 2 in Eq. (34) comes from the initial conditions for the two-exciton state, i.e., $\rho_{P_2',P_2'}(0) = 1$ and otherwise zero.

We will now discuss the characteristic behaviors described by Eqs. (32) and (34) using a CuCl quantum-cube system that has the coupling strengths calculated in Sec. II: $\hbar U = 89\ \mu$eV and $\hbar U' = 14\ \mu$eV. Figure 5(a) shows the temporal evolution of the output population $\rho_{P_1,P_1}(t)$ for some energy differences $\Delta\Omega$. The fastest energy transfer is observed for the condition $\Delta\Omega = U$ (dotted curve), where the population can reach half of the maximum value. This is because the coherent operation part couples with the output part in the one-exciton state via states $|S_1\rangle$ and $|P_1'\rangle$. However, state $|S_1\rangle$ is not fully occupied when we set the initial condition so that only one quantum cube is excited independently. In other words, state $|A_1\rangle$, which decouples state $|P_1'\rangle$ in a symmetric system, is excited simultaneously, and the population remains in the same state $|A_1\rangle$ without temporal evolution. Conversely, for two-exciton states [Fig. 5(b)], the energy transfer occurs under the resonance condition $\Delta\Omega = -U$ and the population can reach unity because the initial state $|P_2'\rangle$ is independent of state $|A_2'\rangle$.

The steepness of the resonance determines the contrast of the output signal. In Fig. 6, the population at $t = 100$ ps, which is the time until energy transfer is almost completed under resonance conditions $\Delta\Omega = \pm U$, is plotted as a function of the energy difference $\Delta\Omega$ for the one- and two-exciton states, as shown by the solid and dashed curves, respectively. We clearly find that two types of switching operations can be realized by choosing the appropriate energy difference $\Delta\Omega = \pm U$. From Eqs. (32) and (34), narrow

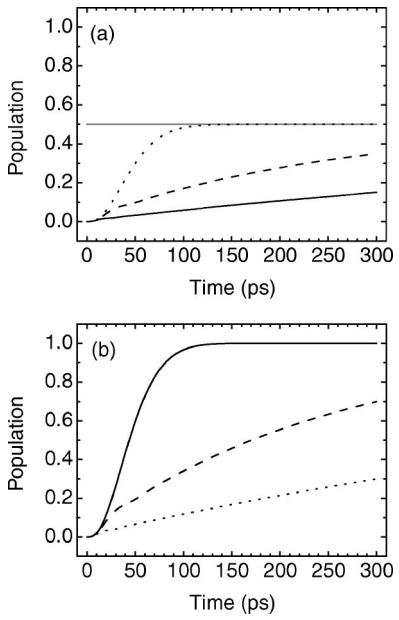

FIG. 5. Temporal evolution of the output populations for (a) one- and (b) two-exciton states. The solid, dashed, and dotted curves represent the results for the energy difference $\Delta\Omega=-U$, 0, and U, respectively. The parameters are set to $\hbar U=89\ \mu$eV, $\hbar U'=14\ \mu$eV, and $\Gamma^{-1}=10$ ps. The output population for the one-exciton state does not exceed a value of 0.5 (the horizontal gray line) because of the initial conditions.

peaks are obtained when $W_+\ll 1$ and $W_-=0$, i.e., $2\sqrt{2}U'\sim\Gamma/2\ll 1$. In this case, a high contrast logic operation can be achieved.

These results are summarized in Table I, which shows the logic operations inherent in nanophotonic devices using typical coherent process and the process with decoherence that occur in a quantum-dot system. The system behaves as an AND-logic gate when the energy difference is set to $\Delta\Omega=-U$, and the system provides an XOR-like-logic operation when $\Delta\Omega=U$. The value 0.5 indicates that the signal can be detected at a 1/2 probability level. As explained in the Introduction, these operations are different from the quantum logic, and long quantum coherence time is unnecessary. The

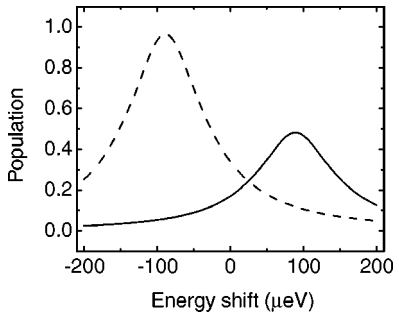

FIG. 6. Variation in the output populations at a fixed time of $t=100$ ps as a function of the energy difference $\Delta\Omega$. The solid and dashed curves represent the one- and two-exciton states, respectively. The optical near-field coupling strengths $\hbar U$ and $\hbar U'$ and the nonradiative relaxation constant Γ have the same values as in Fig. 5.

TABLE I. Relationship between the input and output populations for the energy difference $\Delta\Omega=\pm U$.

Input		Output: C	
A	B	$\Delta\Omega=-U$	$\Delta\Omega=U$
0	0	0	0
1	0	0	0.5
0	1	0	0.5
1	1	1	0

critical limit of these logic gates is determined by the following condition; the energy-transfer time from the coherent operation part to the output part, which is estimated about 50 ps for the CuCl quantum-cube system, is enough shorter than the radiative lifetime ($\sim$1 ns) of excitons in each quantum dot.

IV. EFFECTS OF ASYMMETRY ON EXCITON DYNAMICS

It is valuable to examine the exciton dynamics in an asymmetrically arranged quantum-dot system to estimate the fabrication tolerance for the system described above and to propose further functional operations inherent in nanophotonic devices. In this section, we demonstrate the effects of asymmetry numerically. In addition, we comment on a positive use of these effects, i.e., the possibility of accessing quantum entangled states depending on the prepared initial excitation in a quantum-dot system. The simultaneous differential equations in an asymmetric system are given in part by

$$\dot{\rho}_{S_1,S_1}(t)=i\sqrt{2}\overline{U}'[\rho_{S_1,P_1'}(t)-\rho_{P_1',S_1}(t)]+i\Delta\Omega_{AB}[\rho_{S_1,A_1}(t)-\rho_{A_1,S_1}(t)],$$

$$\dot{\rho}_{S_1,P_1'}(t)=\left\{i(\Delta\Omega-U)-\frac{\Gamma}{2}\right\}\rho_{S_1,P_1'}(t)+i\sqrt{2}\overline{U}'[\rho_{S_1,S_1}(t)-\rho_{P_1',P_1'}(t)]-i\sqrt{2}\Delta U'\rho_{S_1,A_1}(t)-i\Delta\Omega_{AB}\rho_{A_1,P_1'}(t),$$

$$\dot{\rho}_{A_1,A_1}(t)=i\sqrt{2}\Delta U'[\rho_{P_1',A_1}(t)-\rho_{A_1,P_1'}(t)]-i\Delta\Omega_{AB}[\rho_{S_1,A_1}(t)-\rho_{A_1,S_1}(t)],$$

$$\dot{\rho}_{A_1,P_1'}(t)=\left\{i(\Delta\Omega+U)-\frac{\Gamma}{2}\right\}\rho_{A_1,P_1'}(t)+i\sqrt{2}\overline{U}'\rho_{A_1,S_1}(t)-i\sqrt{2}\Delta U'[\rho_{A_1,A_1}(t)-\rho_{P_1',P_1'}(t)]-i\Delta\Omega_{AB}\rho_{S_1,P_1'}(t),\tag{36}$$

for the one-exciton states, and

$$\dot{\rho}_{S_2',S_2'}(t) = -\Gamma\rho_{S_2',S_2'}(t) + i\sqrt{2}\overline{U}'[\rho_{S_2',P_2'}(t) - \rho_{P_2',S_2'}(t)] + i\Delta\Omega_{AB}[\rho_{S_2',A_2'}(t) - \rho_{A_2',S_2'}(t)],$$

$$\dot{\rho}_{S_2',P_2'}(t) = \left\{-i(\Delta\Omega + U) - \frac{\Gamma}{2}\right\}\rho_{S_2',P_2'}(t) + i\sqrt{2}\overline{U}'[\rho_{S_2',S_2'}(t) - \rho_{P_2',P_2'}(t)] + i\sqrt{2}\Delta U'\rho_{S_2',A_2'}(t) - i\Delta\Omega_{AB}\rho_{A_2',P_2'}(t),$$

$$\dot{\rho}_{A_2',A_2'}(t) = -\Gamma\rho_{A_2',A_2'}(t) - i\sqrt{2}\Delta U'[\rho_{P_2',A_2'}(t) - \rho_{A_2',P_2'}(t)] - i\Delta\Omega_{AB}[\rho_{S_2',A_2'}(t) - \rho_{A_2',S_2'}(t)],$$

$$\dot{\rho}_{A_2',P_2'}(t) = \left\{-i(\Delta\Omega - U) - \frac{\Gamma}{2}\right\}\rho_{A_2',P_2'}(t) + i\sqrt{2}\overline{U}'\rho_{A_2',S_2'}(t) + i\sqrt{2}\Delta U'[\rho_{A_2',A_2'}(t) - \rho_{P_2',P_2'}(t)] - i\Delta\Omega_{AB}\rho_{S_2',P_2'}(t), \quad (37)$$

for the two-exciton states. Here, we only present the equations that differ from Eqs. (30) and (31) (see the Appendix for more details), and we redefine the parameters $\Delta\Omega = \Omega_{C_2} - (\Omega_A + \Omega_B)/2$, $\Delta\Omega_{AB} = \Omega_A - \Omega_B$, $\overline{U}' = (U_{BC} + U_{CA})/2$, and $\Delta U' = (U_{BC} - U_{CA})/2$. In the asymmetric system, the exciton dynamics between states $|S\rangle$ and $|P\rangle$ do not change, provided the coupling strength U' for a symmetric system is replaced by the average value $\overline{U}'$ in Eqs. (36) and (37). The main difference is that the matrix elements for states $|A\rangle$ can couple with states $|S\rangle$ and $|P\rangle$ in an asymmetric system, while these are decoupled in a symmetric system. Two types of coupling emerge in an asymmetric system: one originates from the energy difference $\Delta\Omega_{AB}$ between QD-A and -B, and the other comes from the arrangement of the three quantum dots, which is expressed using the parameter $\Delta U'$. Previously,[17] we discussed the influence of the energy difference on the exciton dynamics in a two-quantum-dot system that mainly degrades the signal contrast. Here, we focus on the effects of asymmetry due to the arrangement of each quantum dot, assuming $\Delta\Omega_{AB} = 0$.

In order to examine the effects of the quantum-dot arrangement, the average coupling strength $\overline{U}'$ is fixed so that states $|S\rangle$ and $|P\rangle$ maintain the same temporal evolution that was found in the symmetric system. Then, the difference between the coupling strengths $\Delta U'$ varies from 0 to $\pm U$, where the exciton dynamics are independent of the sign of $\Delta U'$. Therefore, an asymmetry factor is defined by the ratio of $|\Delta U'|$ to $\overline{U}'$, varying from 0 (symmetry) to 1 (maximum amount of asymmetry).

Figure 7 presents the temporal evolution of the output population for the energy difference $\Delta\Omega = -U$ (an AND-logic gate case) with and without an asymmetric arrangement. For the one-exciton state [Fig. 7(a)], the asymmetric arrangement strongly affects the exciton dynamics, and the OFF state in the AND-gate operation is no longer valid because the off-resonance condition for the energy transfer between states $|S_1\rangle$ and $|P_1'\rangle$ acts oppositely to the resonance condition between states $|A_1\rangle$ and $|P_1'\rangle$. This is evident in Eq. (36), for example, by comparing the matrix elements $\rho_{S_1,P_1'}(t)$ with $\rho_{A_1,P_1'}(t)$. Therefore, in the one-exciton state, the exciton population is very sensitive to the asymmetric arrangement. By contrast, the two-exciton state is not influenced by the quantum-dot arrangement [see Fig. 7(b)]. We also observe small and high-frequency oscillations for the dashed and dotted curves ($|\Delta U'|/\overline{U}' = 0.5$ and 1.0) in Fig. 7(a). These come from the coherence between states $|S_1\rangle$ and $|A_1\rangle$ which can be seen in the equations of motion of $\rho_{S_1,A_1}(t)$ and $\rho_{A_1,S_1}(t)$ [see Eq. (A1)]. Since the coherence is always excited by mediating state $|P_1'\rangle$ and the state $|P_1'\rangle$ has a short lifetime dominated by the relaxation constant Γ, the oscillations have no relation to the population dynamics. Figure 8 shows the variation in the output population at $t = 100$ ps as a function of the asymmetry factor $|\Delta U'|/\overline{U}'$. From this figure, it follows that the asymmetry only affects the one-exciton state, where it breaks the OFF state in the logic gate, as shown by the curve with squares, and the signal contrast decreases with increasing asymmetry.

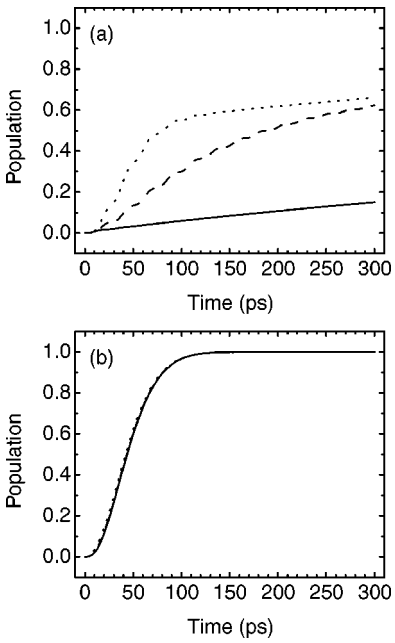

FIG. 7. Temporal evolution of the output populations where the energy difference is set to $\Delta\Omega = -U$ ($\hbar U = 89$ μeV). Parts (a) and (b) show the populations for one- and two-exciton states, respectively. The solid, dashed, and dotted curves represent the results for asymmetry factors $|\Delta U'|/\overline{U}' = 0$, 0.5, and 1.0, respectively, where the average coupling strength is set to $\hbar\overline{U}' = 14$ μeV. In part (b), the three curves are almost identical.

Conversely, for the XOR-logic gate ($\Delta\Omega = U$), the two-exciton states correspond to the off-resonant states in the symmetric system. Therefore, the excitation is transferred to the output energy level in QD-C as the asymmetry factor increases, as shown in Fig. 9(b). Similarly, the variation in the output population with the asymmetry factor is plotted in

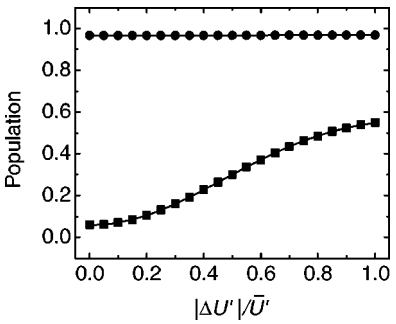

FIG. 8. Variation in the output populations at a fixed time of $t = 100$ ps as a function of the asymmetry factor, where the energy difference is set to $\Delta\Omega = -U$ ($\hbar U = 89$ μeV) and an average coupling strength of $\hbar\bar{U}' = 14$ μeV is used. The curves shown with square and circular dots represent the one- and two-exciton states, respectively. Only the exciton population in the one-exciton state is modified by increasing the asymmetry factor.

Fig. 10, where the time is fixed at $t = 100$ ps. The figure shows that the XOR-logic operation in the symmetric system is reversed when the asymmetry factor exceeds 0.5 because a one-exciton state can occupy the initial state of $|S_1\rangle$ with a probability of 1/2, as shown in Sec. III. Consequently, the output population also reaches a probability of 1/2. This is also valid in the asymmetric system. However, the asymmetric arrangement enables coupling of the two-exciton states $|P_2'\rangle$ and $|A_2'\rangle$. State $|P_2'\rangle$ can be fully excited in the initial stage, so the output population reaches a unit value via states $|A_2'\rangle$. This exceeds the output population 0.5 for a one-exciton state with a larger amount of asymmetry.

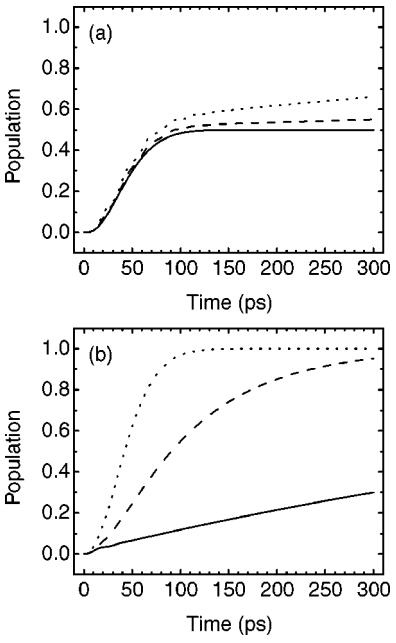

FIG. 9. Temporal evolution of the output populations for the energy difference of $\Delta\Omega = U$ ($\hbar U = 89$ μeV). Parts (a) and (b) show the populations for the one- and two-exciton states, respectively. The solid, dashed, and dotted curves represent the results for asymmetry factors $|\Delta U'|/\bar{U}' = 0$, 0.5, and 1.0, respectively, where the average coupling strength is set to $\hbar\bar{U}' = 14$ μeV.

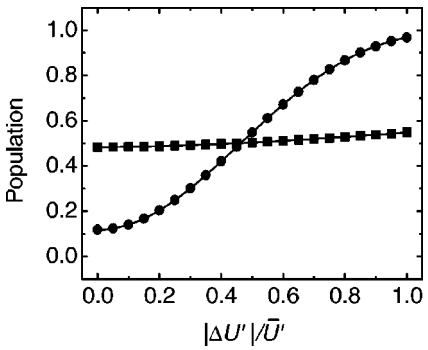

FIG. 10. Variation in the output populations at the fixed time of $t = 100$ ps as a function of the asymmetry factor, where the energy difference is set to $\Delta\Omega = U$ ($\hbar U = 89$ μeV) and an average coupling strength of $\hbar\bar{U}' = 14$ μeV is used. The curves shown with square and circular dots represent the one- and two-exciton states, respectively. The exciton population in the two-exciton state exceeds that of the one-exciton state when the asymmetry factor $|\Delta U'|/\bar{U}'$ exceeds 0.5, so the XOR-logic operation is reversed.

An asymmetric system can also be applied to inherent nanophotonic functions. As mentioned above, the effect of asymmetry is based on coupling to states $|A\rangle$, which are similar to the so-called ''dark states'' in an asymmetric system.[25] In other words, the populations of states $|S\rangle$ and $|A\rangle$ can be chosen selectively by adjusting the arrangement of some of the quantum dots. Note that both states are expressed by the superposition of eigenstates in isolated (noninteracting) quantum dots. Therefore, a system composed of three quantum dots cannot only select information that depends on the initially prepared excitations, but also information that reflects the initial quantum entangled states in the coherent operation part. From this perspective, such nanophotonic devices are useful in connecting quantum devices as a detector and interface devices which identify occupation probability of the quantum entangled states in an input signal.

V. CONCLUSIONS

This paper proposed nanophotonic inherent operations using a three-quantum-dot system. Such a system consists of a coherent operation part and an incoherent output part. The exciton state in the coherent operation part can be read selectively by adjusting the energy level in an output quantum dot or the size of the quantum dot. First, we derived the coupling strength induced by an optical near field and showed that optical near-field coupling enables us to access dipole-forbidden energy levels for conventional far-field light. Then, we derived the equations of motion for the exciton dynamics in a symmetric system to discuss the coupling properties between the coherent operation part and the output part. Initially prepared one- and two-exciton states couple resonantly with the output part due to the optical near-field coupling when the energy level in the third quantum dot is set higher than one and lower than in the other identical quantum dots. This feature is applicable to logic operations. Using analytical solutions, we showed that the

system operates as an AND-logic gate when the energy difference is $\Delta\Omega=-U$, and it operates as an XOR-logic gate when $\Delta\Omega=U$. Furthermore, we examined the effects of asymmetry due to the arrangement of quantum dots numerically. The asymmetry allows coupling between states $|A\rangle$ and $|P\rangle$, and $|A\rangle$ and $|S\rangle$; these states are decoupled in the symmetric system. Although the asymmetric arrangement decreases the signal contrast in the AND- and XOR-logic operations, it introduces a technique to manipulate the information about quantum entangled states or quantum coherence by adjusting the quantum-dot arrangement. In conclusion, we proposed functional operations (AND- and XOR-logic gates) using a near-field optically coupled quantum-dot system and characteristic device operations inherent in nanophotonics, including coherent and dissipative process. Such a system opens up a different way to nanoscale science and technology.

ACKNOWLEDGMENTS

The authors thank Dr. T. Kawazoe (Japan Science and Technology Agency) for kindly providing experimental information about CuCl quantum dots and the dynamics driven by optical near-field interactions.

APPENDIX: EQUATIONS OF MOTION IN AN ASYMMETRIC SYSTEM

The equations of motion for density-matrix elements in an asymmetric system are derived using the bases described in Eqs. (25) and (26) for one-exciton states,

$$\dot{\rho}_{S_1,S_1}(t)=i\sqrt{2}\overline{U}'[\rho_{S_1,P_1'}(t)-\rho_{P_1',S_1}(t)]+i\Delta\Omega_{AB}[\rho_{S_1,A_1}(t)-\rho_{A_1,S_1}(t)],$$

$$\dot{\rho}_{S_1,P_1'}(t)=\left\{i(\Delta\Omega-U)-\frac{\Gamma}{2}\right\}\rho_{S_1,P_1'}(t)+i\sqrt{2}\overline{U}'[\rho_{S_1,S_1}(t)-\rho_{P_1',P_1'}(t)]-i\sqrt{2}\Delta U'\rho_{S_1,A_1}(t)-i\Delta\Omega_{AB}\rho_{A_1,P_1'}(t),$$

$$\dot{\rho}_{P_1',S_1}(t)=\left\{-i(\Delta\Omega-U)-\frac{\Gamma}{2}\right\}\rho_{P_1',S_1}(t)-i\sqrt{2}\overline{U}'[\rho_{S_1,S_1}(t)-\rho_{P_1',P_1'}(t)]+i\sqrt{2}\Delta U'\rho_{A_1,S_1}(t)+i\Delta\Omega_{AB}\rho_{P_1',A_1}(t),$$

$$\dot{\rho}_{P_1',P_1'}(t)=-\Gamma\rho_{P_1',P_1'}(t)-i\sqrt{2}\overline{U}'[\rho_{S_1,P_1'}(t)-\rho_{P_1',S_1}(t)]-i\Delta U'[\rho_{P_1',A_1}(t)-\rho_{A_1,P_1'}(t)],$$

$$\dot{\rho}_{P_1',A_1}(t)=\left\{-i(\Delta\Omega+U)-\frac{\Gamma}{2}\right\}\rho_{P_1',A_1}(t)-i\sqrt{2}\overline{U}'\rho_{S_1,A_1}(t)+i\sqrt{2}\Delta U'[\rho_{A_1,A_1}(t)-\rho_{P_1',P_1'}(t)]+i\Delta\Omega_{AB}\rho_{P_1',S_1}(t),$$

$$\dot{\rho}_{A_1,P_1'}(t)=\left\{i(\Delta\Omega+U)-\frac{\Gamma}{2}\right\}\rho_{A_1,P_1'}(t)+i\sqrt{2}\overline{U}'\rho_{A_1,S_1}(t)-i\sqrt{2}\Delta U'[\rho_{A_1,A_1}(t)-\rho_{P_1',P_1'}(t)]-i\Delta\Omega_{AB}\rho_{S_1,P_1'}(t),$$

$$\dot{\rho}_{S_1,A_1}(t)=-i2U\rho_{S_1,A_1}(t)-i\sqrt{2}\overline{U}'\rho_{P_1',A_1}(t)-i\sqrt{2}\Delta U'\rho_{S_1,P_1'}(t)+i\Delta\Omega_{AB}[\rho_{S_1,S_1}(t)-\rho_{A_1,A_1}(t)],$$

$$\dot{\rho}_{A_1,S_1}(t)=i2U\rho_{A_1,S_1}(t)+i\sqrt{2}\overline{U}'\rho_{A_1,P_1'}(t)+i\sqrt{2}\Delta U'\rho_{P_1',S_1}(t)-i\Delta\Omega_{AB}[\rho_{S_1,S_1}(t)-\rho_{A_1,A_1}(t)],$$

$$\dot{\rho}_{A_1,A_1}(t)=i\sqrt{2}\Delta U'[\rho_{P_1',A_1}(t)-\rho_{A_1,P_1'}(t)]-i\Delta\Omega_{AB}[\rho_{S_1,A_1}(t)-\rho_{A_1,S_1}(t)], \tag{A1}$$

where $\Delta\Omega=\Omega_{C_2}-(\Omega_A+\Omega_B)/2$, $\Delta\Omega_{AB}=\Omega_A-\Omega_B$, $\overline{U}'=(U_{BC}+U_{CA})/2$, and $\Delta U'=(U_{BC}-U_{CA})/2$. For two-exciton states,

$$\dot{\rho}_{S_2',S_2'}(t)=-\Gamma\rho_{S_2',S_2'}(t)+i\sqrt{2}\overline{U}'[\rho_{S_2',P_2'}(t)-\rho_{P_2',S_2'}(t)]+i\Delta\Omega_{AB}[\rho_{S_2',A_2'}(t)-\rho_{A_2',S_2'}(t)],$$

$$\dot{\rho}_{S_2',P_2'}(t)=\left\{-i(\Delta\Omega+U)-\frac{\Gamma}{2}\right\}\rho_{S_2',P_2'}(t)+i\sqrt{2}\overline{U}'[\rho_{S_2',S_2'}(t)-\rho_{P_2',P_2'}(t)]+i\sqrt{2}\Delta U'\rho_{S_2',A_2'}(t)-i\Delta\Omega_{AB}\rho_{A_2',P_2'}(t),$$

$$\dot{\rho}_{P_2',S_2'}(t)=\left\{i(\Delta\Omega+U)-\frac{\Gamma}{2}\right\}\rho_{P_2',S_2'}(t)-i\sqrt{2}\overline{U}'[\rho_{S_2',S_2'}(t)-\rho_{P_2',P_2'}(t)]-i\sqrt{2}\Delta U'\rho_{A_2',S_2'}(t)+i\Delta\Omega_{AB}\rho_{P_2',A_2'}(t),$$

$$\dot{\rho}_{P_2',P_2'}(t)=-i\sqrt{2}\overline{U}'[\rho_{S_2',P_2'}(t)-\rho_{P_2',S_2'}(t)]+i\sqrt{2}\Delta U'[\rho_{P_2',A_2'}(t)-\rho_{A_2',P_2'}(t)],$$

$$\dot{\rho}_{A_2',P_2'}(t)=\left\{-i(\Delta\Omega-U)-\frac{\Gamma}{2}\right\}\rho_{A_2',P_2'}(t)+i\sqrt{2}\overline{U}'\rho_{A_2',S_2'}(t)+i\sqrt{2}\Delta U'[\rho_{A_2',A_2'}(t)-\rho_{P_2',P_2'}(t)]-i\Delta\Omega_{AB}\rho_{S_2',P_2'}(t),$$

$$\dot{\rho}_{P_2',A_2'}(t)=\left\{i(\Delta\Omega-U)-\frac{\Gamma}{2}\right\}\rho_{P_2',A_2'}(t)-i\sqrt{2}\overline{U}'\rho_{S_2',A_2'}(t)-i\sqrt{2}\Delta U'[\rho_{A_2',A_2'}(t)-\rho_{P_2',P_2'}(t)]+i\Delta\Omega_{AB}\rho_{P_2',S_2'}(t),$$

$$\dot{\rho}_{S_2',A_2'}(t)=(-i2U-\Gamma)\rho_{S_2',A_2'}(t)-i\sqrt{2}\overline{U}'\rho_{P_2',A_2'}(t)+i\sqrt{2}\Delta U'\rho_{S_2',P_2'}(t)+i\Delta\Omega_{AB}[\rho_{S_2',S_2'}(t)-\rho_{A_2',A_2'}(t)],$$

$$\dot{\rho}_{A_2',S_2'}(t)=(i2U-\Gamma)\rho_{A_2',S_2'}(t)+i\sqrt{2}\overline{U}'\rho_{A_2',P_2'}(t)-i\sqrt{2}\Delta U'\rho_{P_2',S_2'}(t)-i\Delta\Omega_{AB}[\rho_{S_2',S_2'}(t)-\rho_{A_2',A_2'}(t)],$$

$$\dot{\rho}_{A_2',A_2'}(t)=-\Gamma\rho_{A_2',A_2'}(t)-i\sqrt{2}\Delta U'[\rho_{P_2',A_2'}(t)-\rho_{A_2',P_2'}(t)]-i\Delta\Omega_{AB}[\rho_{S_2',A_2'}(t)-\rho_{A_2',S_2'}(t)]. \quad \text{(A2)}$$

*Electronic address: suguru.sangu@nts.ricoh.co.jp

[1] M. Ohtsu, in *Near-Field Optics: Principles and Applications*, edited by X. Zhu and M. Ohtsu (World Scientific, Singapore, 2000), pp. 1–8.

[2] M. Ohtsu, K. Kobayashi, T. Kawazoe, S. Sangu, and T. Yatsui, IEEE J. Sel. Top. Quantum Electron. **8**, 839 (2002).

[3] *Near-Field Nano/Atom Optics and Technology*, edited by M. Ohtsu (Springer-Verlag, Tokyo, 1998).

[4] K. Matsuda, K. Ikeda, T. Saiki, H. Tsuchiya, H. Saito, and K. Nishi, Phys. Rev. B **63**, 121304 (2001).

[5] K. Matsuda, T. Saiki, S. Nomura, M. Mihara, Y. Aoyagi, S. Nair, and T. Takagahara, Phys. Rev. Lett. **91**, 177401 (2003).

[6] T. Yatsui, M. Kourogi, and M. Ohtsu, Appl. Phys. Lett. **79**, 4583 (2001).

[7] N. Hosaka and T. Saiki, J. Microsc. **202**, 362 (2001).

[8] R.U. Maheswari, S. Mononobe, K. Yoshida, M. Yoshimoto, and M. Ohtsu, Jpn. J. Appl. Phys., Part 1 **38**, 6713 (1999).

[9] T. Kawazoe, K. Kobayashi, J. Lim, Y. Narita, and M. Ohtsu, Phys. Rev. Lett. **88**, 067404 (2002).

[10] C.D. Simserides, U. Hohenester, G. Goldoni, and E. Molinari, Phys. Rev. B **62**, 13 657 (2000).

[11] K. Cho, Y. Ohfuti, and K. Arima, Surf. Sci. **363**, 378 (1996).

[12] G.W. Bryant, Appl. Phys. Lett. **72**, 768 (1998).

[13] K. Kobayashi and M. Ohtsu, J. Microsc. **194**, 249 (1999).

[14] A. Shojiguchi, K. Kobayashi, S. Sangu, K. Kitahara, and M. Ohtsu, Nonlinear Opt. **29**, 563 (2002).

[15] A. Shojiguchi, K. Kobayashi, S. Sangu, K. Kitahara, and M. Ohtsu, J. Phys. Soc. Jpn. **72**, 2984 (2003).

[16] T. Kawazoe, K. Kobayashi, S. Sangu, and M. Ohtsu, Appl. Phys. Lett. **82**, 2957 (2003).

[17] S. Sangu, K. Kobayashi, T. Kawazoe, A. Shojiguchi, and M. Ohtsu, J. Appl. Phys. **93**, 2937 (2003).

[18] K. Kobayashi, S. Sangu, A. Shojiguchi, T. Kawazoe, K. Kitahara, and M. Ohtsu, J. Microsc. **210**, 247 (2003).

[19] H. Hori, in *Optical and Electronic Process of Nano-Matters*, edited by M. Ohtsu (KTK Scientific, Tokyo/Kluwer Academic, Dordecht, 2001), pp. 1–55.

[20] S.D. Rinaldis, I. D'Amico, and F. Rossi, Appl. Phys. Lett. **81**, 4236 (2002).

[21] F. Troiani, U. Hohenester, and E. Molinari, Phys. Rev. B **65**, 161301 (2002).

[22] E. Biolatti, R.C. Iotti, P. Zanardi, and F. Rossi, Phys. Rev. Lett. **85**, 5647 (2000).

[23] L. Quiroga and N.F. Johnson, Phys. Rev. Lett. **83**, 2270 (1999).

[24] T. Förster, in *Modern Quantum Chemistry*, edited by O. Sinanoğlu (Academic Press, London, 1965), pp. 93–137.

[25] M.O. Scully and M.S. Zubairy, *Quantum Optics* (Cambridge University Press, Cambridge, 1997).

[26] P. Zanardi and F. Rossi, Phys. Rev. Lett. **81**, 4752 (1998).

[27] M. Thorwart and P. Hănggi, Phys. Rev. A **65**, 012309 (2001).

[28] C. Cohen-Tannoudji, J. Depont-Roc, and G. Grynberg, *Photons and Atoms: Introduction to Quantum Electrodynamics* (Wiley, New York, 1989).

[29] D.P. Craig and T. Thirunamachandran, *Molecular Quantum Electrodynamics* (Academic Press, London, 1984).

[30] J. Knoester and S. Mukamel, Phys. Rev. A **39**, 1899 (1989).

[31] J.R. Zurita-Sanchez and L. Novotny, J. Opt. Soc. Am. B **19**, 1355 (2002).

[32] K. Kobayashi, S. Sangu, H. Ito, and M. Ohtsu, Phys. Rev. A **63**, 013806 (2001).

[33] S. Sangu, K. Kobayashi, and M. Ohtsu, J. Microsc. **202**, 279 (2001).

[34] M. Ohtsu and K. Kobayashi, *Optical Near Fields: Introduction to Classical and Quantum Theories of Electromagnetic Phenomena at the Nanoscale* (Springer-Verlag, Berlin, 2004).

[35] E. Hanamura, Phys. Rev. B **37**, 1273 (1988).

[36] B. Coffey, Phys. Rev. A **17**, 1033 (1978).

[37] H.J. Carmichael, *Statistical Methods in Quantum Optics 1* (Springer-Verlag, Berlin, 1999).